JOURNAL OF MATERIALS SCIENCE 25 (1990) 2063–2070

Formation and growth morphology of oxidation-induced ferrite layer in Fe–Mn–Al–Cr–C alloys

J. G. DUH, C. J. WANG
Department of Materials Science and Engineering, National Tsing Hua University, Hsinchu, Taiwan

Three austenitic Fe–31Mn–9Al–xCr–0.87C alloys (x = 0, 3 and 6) have been oxidized in dry air at 800 to 1100° C. An oxidation-induced ferrite layer is observed between the oxide layer and the austenite matrix. The ferrite layer is formed due to the selective oxidation of manganese. Qualitative and quantitative electron microscopic techniques are employed to investigate the morphological development and elemental redistribution in the alloy system. The mechanism of the formation and growth of the ferrite layer and the diffusion path of the carbon due to austenitic decomposition are explored.

1. Introduction

In past years, many research activities have focused on development of the potential of Fe–Mn–Al-based alloys. Several investigators studied the high-temperature oxidation behaviour of the Fe–Mn–Al system [1–7]. Manganese and carbon are austenite stabilizers in the Fe–Mn–Al–C alloy system. However, due to the decarburization of iron-base alloys and the selective oxidation of manganese in this alloy system, both manganese and carbon are found to be detrimental to the high-temperature resistance [4, 8–10]. During high-temperature oxidation a ferrite layer has been observed between the oxide scale and austenitic alloy matrix in several high-manganese and high-carbon alloy systems [11–17]. An oxidation-induced ferrite layer was observed in Fe–31Mn–9Al–3Cr–0.87C alloy oxidized at 800 and 1000° C [16]. The diffusivity of manganese in the ferrite layer at 1000° C was evaluated with a proposed diffusion-related formulation [17]. Recently, kinetic evolution and morphological development in the oxidation of Fe–Mn–Al–Cr–C alloys was investigated [18]. Whether the formation of the ferrite layer is dominated by decarburization or by the selective oxidation of manganese is, however, left unanswered. The purpose of this study is to investigate the kinetics and mechanisms involved in the formation and growth of the ferrite layer in the Fe–Mn–Al–Cr–C alloy system. Electron microscopic techniques are employed to study the elemental redistribution during high-temperature oxidation. The roles played by carbon migration and the selective oxidation of manganese are explored.

2. Experimental procedure

The chemical compositions of the alloys employed in these studies are listed in Table I. The alloys were prepared from high-purity materials and melted in an argon-shielded induction furnace. The details of the specimen preparation and oxidation experiment were described elsewhere [18]. Phases present in the specimen were identified by X-ray diffraction. The morphologies of the oxide and alloy substrate were examined with both the optical microscope (OM) and scanning electron microscope (SEM). Elemental redistribution was detected through an X-ray map technique, and qualitative line scanning for the carbon characteristic X-ray was achieved with the STE analysing crystal with a computerized electron microprobe (Jeol JCXA-733). Quantitative analysis of the concentration for iron, manganese, aluminium and chromium was performed with the aid of a ZAF-corrected program. To investigate the phases and structures existing at high temperatures, two different heat treatments, i.e. air cooling and water quenching, were studied. The air-cooled specimens were studied morphologically, and the water-quenched specimens used for concentration profile measurements.

3. Results

All three alloys employed in this study have similar oxidation morphologies at 800° C, which include bulky oxides, an austenitic matrix and a ferrite layer between the oxide layer and alloy matrix after the early stage of oxidation. The major difference between alloys with and without chromium addition is that more chromium carbide is formed in the matrix for the higher-chromium alloy.

As the oxidation time is increased, a ferrite layer and wavy matrix–ferrite and ferrite–oxide interfaces are observed. The width of the ferrite is estimated to be 5 μm for alloy A oxidized for 24 h. A typical morphology of the chromium-containing alloys B and C is shown in Fig. 1. Isolated and fine chromium carbides are dispersed at the oxide–ferrite interface as well as the innermost oxide layer. For alloy B oxidized after 24 h the width of the ferrite layer is about 24 μm. The morphology of alloy C is similar to that of alloy B as

0022–2461/90 $03.00 + .12

TABLE I Chemical compositions of alloys employed in this study

Alloy	Composition (wt %)				
	Mn	Al	Cr	C	Fe
A	31.18	8.69	–	0.87	Bal.
B	31.30	8.92	5.96	0.86	Bal.
C	30.95	8.87	2.98	0.87	Bal.

TABLE II Width of ferrite layer for alloy C oxidized at 800° C

Time (h)	Layer thickness (μm)
24	13.6 ± 6.1
48	20.8 ± 5.7
120	28.3 ± 10.3
250	54.2 ± 11.8

shown in Fig. 1. The number of fine chromium carbide particles beneath the oxide layer and the carbide fringes in the ferrite layer are, however, decreased for alloy C. The nuclei of the ferrite phase are first observed after 12 h. After 24 h a continuous ferrite layer is formed and separates the oxide layer from the alloy matrix. The widths of the ferrite layers after 24 h oxidation are summarized in Table II.

For alloy A oxidized at 1000° C two categories of oxide morphology are observed. The first shows a nearly planar interface between the ferrite layer and the austenite matrix (Fig. 2). Randomly oriented stringers of Fe_3AlC_x are observed in the ferrite layer [18]. The ferrite layer for alloy A oxidized for 24 hours is about 100 μm. After oxidation for 12 h another type of morphology with large and broad oxide nodules is developed (Fig. 3). Beneath the oxide nodules, the width of the ferrite is relatively thin where the formation of carbide is also reduced. For alloy C oxidized for 12 h a bulky oxide and a planar α–γ interface is the only morphology observed (Fig. 4). In fact, the wavy ferrite layer is first detected at around 9 h of oxidation. The width of the ferrite layer is nearly the same for various cooling rates. The width of the ferrite layer after 12 h oxidation is listed in Table III.

A concentration profile of metallic elements for alloy C oxidized at 1000° C after 24 h followed by water quenching is presented in Fig. 5. It appears that manganese is the only element depleted in the ferrite layer. The manganese contents at the α–γ phase boundary are 31.3 and 17.5 wt % at the γ and α side, respectively. It is interesting to note that according to the X-ray line scan of carbon for the quenched specimen (Fig. 6), there is carbon build-up at the γ side near the α–γ interface. The reason behind this phenomenon will be explored later on.

Oxidation of alloy C at a temperature higher than 1000° C exhibits the same morphology as that for 1000° C. A peninsular bulky oxide is observed at the intersection between the grain boundaries and the oxide layer (Fig. 7a). The concentration profile for the specimen oxidized at 1100° C for 24 h is presented in Fig. 7b. The concentration of manganese gradually declines at the γ side near the α–γ interface. This observation prevails for longer oxidation times. For the 24 h oxidation the concentration of manganese decreases from 15.8 wt % at the γ side of the α–γ phase boundary to 7.43 wt % at the α side of the ferrite–oxide interface.

4. Discussion

4.1. Formation of the ferrite layer

It is argued that the formation of ferrite in the manganese-containing austenitic alloys occurs either due to the selective oxidation of manganese at the oxidation temperature or during the cooling process [8, 9, 11, 12]. Based on the results for the quenched specimens, there is evidence to confirm that the ferrite layer is formed at the oxidation temperature. In the morphology of the quenched alloy C oxidized at 1000° C for 120 h (Fig. 4), a fully ferrite layer is formed between the oxide scale and the austenite matrix. Since the quenching process is intended to freeze the high-temperature structure, the ferrite phase shown in the Fig. 4 indicates that it is already formed at the oxidation temperature. Moreover, the alloying elements cannot diffuse appreciably during the few seconds spanned by the quench process. If the alloy were fully austenitic at the oxidation temperature, the concentration profile would be a continuous curve after quenching. This is, however, not in agreement with the experimental results presented in Figs 5 and 7b, in which abrupt concentrations changes are detected at the phase boundary. In addition, it is well known that the solubility of carbon in the ferritic phase is lower than that in the austenite. The diffusivity of carbon in

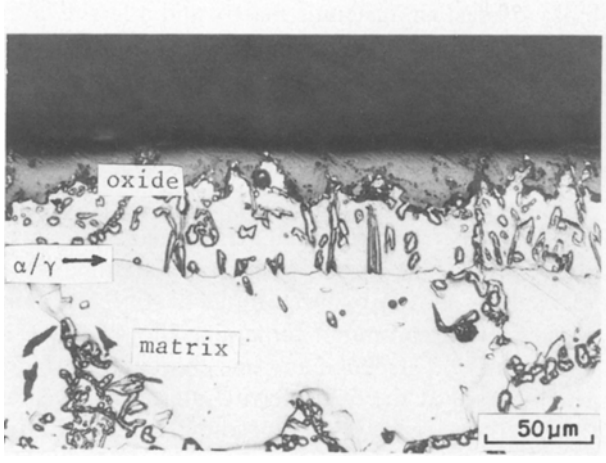

Figure 1 Micrograph of alloy B oxidized at 800° C for 48 h.

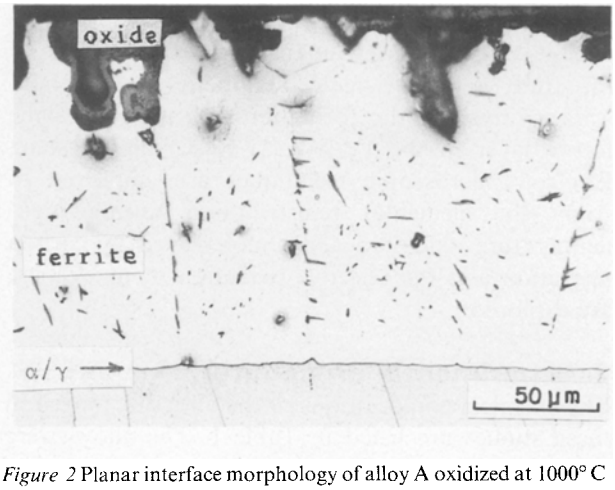

Figure 2 Planar interface morphology of alloy A oxidized at 1000° C for 24 h.

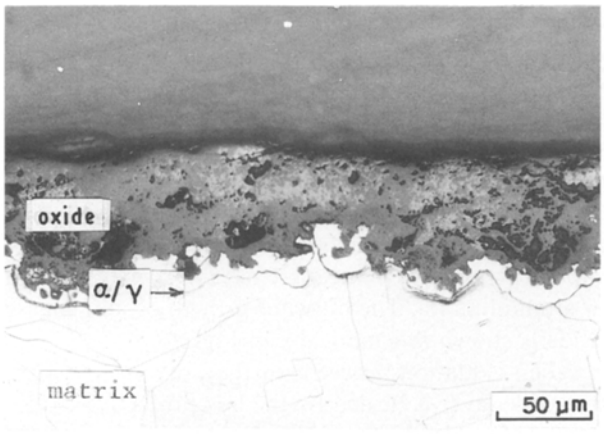

Figure 3 Cross-section of broad oxide nodule with a wavy α–γ interface formed on alloy A oxidized at 1000° C for 24 h.

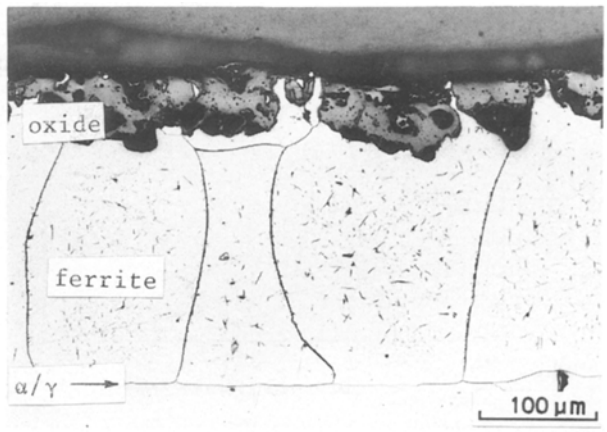

Figure 4 Micrograph of alloy C oxidized at 1000° C for 120 h.

the ferrite phase is, however, larger than that in the austenite. If carbon is not fully depleted during the oxidation and as the $\gamma \rightarrow \alpha$ transformation occurs, carbon in the transformed region would be piled up toward the austenite phase, which is similar to the decomposition of austenite in the Fe–C system [19]. The redistribution of carbon to the austenite side near the ferrite–austenite interface is shown by the X-ray line scan in Fig. 6, in which a pile-up of carbon in the austenite side is observed. Based on the above discussion, it is concluded that the ferrite layer is formed at the oxidation temperature.

Carbon is a strong austenite stabilizer. It is, however, detrimental to the high-temperature oxidation resistance [20, 21]. Due to the high diffusion rate in alloys and the gaseous oxidation products CO and CO_2 for carbon, cavities are usually distributed throughout the oxide layer [22, 23]. Hence decarburization is frequently observed and the oxidation rate is increased as the carbon content increases in the carbon-containing alloys [21]. However, it was reported by Band *et al.* [24] that decarburization could be prevented by an adherent and compact oxide scale. Because of the dissociation pressure of oxides, the oxidation of carbon could be prevented if an adherent layer of Cr_2O_3, MnO, $MnAl_2O_4$, $FeAl_2O_4$ or α-Al_2O_3 was formed. Based on X-ray diffraction identification, oxides other than Cr_2O_3 have been detected in the present study [18]. In addition, it is found that protection and adherence of the oxides do not always prevail at various oxidation temperatures. An adherent oxide scale is observed in the lower temperature range, for example at 800° C. Oxides at temperature lower than 1000° C are found to be less protective. On the other hand, protective oxides such as α-Al_2O_3 and $MnAl_2O_4$ appear at temperatures higher than 1000° C in this study. For the oxidation morphology of 1100° C as seen in Fig. 7, voids appear beneath the oxide layer and decarburization is suggested to occur. As decarburization might take place, the stability of austenite is affected since carbon acts intrinsically as an austenite stabilizer. The selective oxidation of manganese also takes place in this alloy system as shown in Fig. 7b. Thus, whether the formation of the ferrite layer is due to decarburization or selective oxidation of manganese still remains unanswered. In order to resolve the role of both carbon and manganese, schematic representations of the oxidation mechanism are probed in the following paragraphs.

TABLE III Width of ferrite layer for alloy C oxidized at 1000° C

Time (h)	Layer thickness (μm)
12	87.9 ± 9.0
24	144.6 ± 12.0
48	179.9 ± 16.0
120	228.9 ± 19.6

As only a small amount of chromium is added to the Fe–Mn–Al–C-based alloys, the oxidation behaviours of the Fe–Mn–Al–Cr–C alloys are nearly identical to those of Fe–Mn–Al–C alloys. Nevertheless, at temperatures lower than 1000° C chromium carbide can be formed in the chromium-containing alloys. Consequently, the following discussion is divided into two categories according to the chromium carbide formation temperature. The first stage is from 800 to 950° C at which chromium carbide is formed, and the other is above 1000° C at which other types of carbide are observed. The effects of chromium will also be discussed.

4.1.1. Oxidation at 800 to 950° C

Fig. 8 shows the oxide structure of an Fe–Mn–Al alloy with more than 20 wt % Mn oxidized at 800° C at

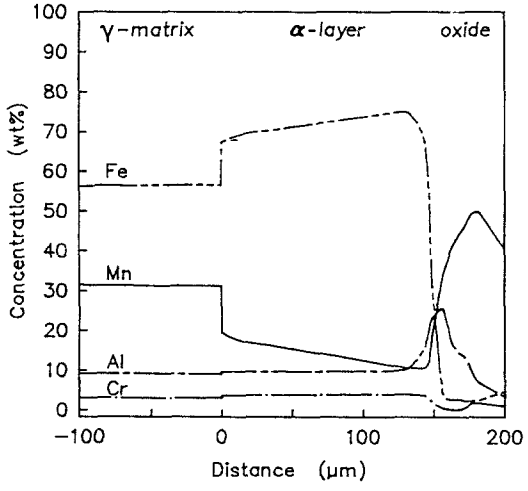

Figure 5 Concentration profiles of metallic elements of alloy C oxidized at 1000° C for 24 h.

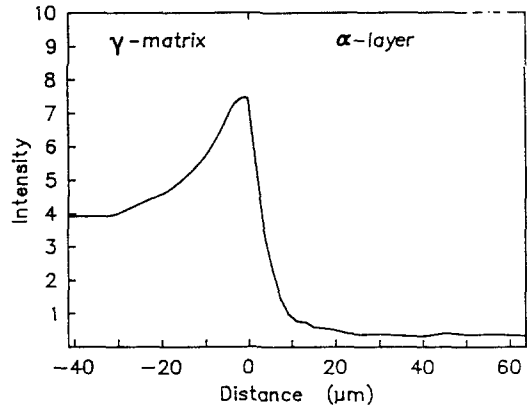

Figure 6 X-ray line scan of carbon at the α–γ interface of alloy C oxidized at 1000° C for 24 h.

200 torr oxygen pressure, as described by Jackson and Wallwork [8]. The same oxide structure is observed in this study for alloy A. There are, however, two differences in the oxide morphology between alloys with and without carbon. For the alloy containing carbon, the oxide nodules are broad and nearly uniform as indicated in Fig. 3. The other distinction is that more voids and cracks are found in alloy A.

A schematic configuration for the stages of growth of bulky oxides and the ferrite layer during oxidation of Fe–Mn–Al–Cr–C alloys is proposed in this study as shown in Fig. 9. At the initial stage of oxidation as indicated in Fig. 9a, porous alumina scale forms over the alloy surface since aluminium acts as a primary oxygen-getter in this alloy system. Carbide is also formed initially at the grain boundary, which is a favourable site for carbide nucleation. In fact, decarburization plays a major role during the early stage of oxidation, since a carbide-free zone of about 100 μm is observed in alloy B oxidized at 800° C for 1 h [18] (Fig. 10a). It is argued that decarburization occurs mostly by means of volume diffusion, since the thickness of the oxide layer at the intersection of grain boundaries is less than that formed along the grain boundary in the alloy matrix (Fig. 10b). On scanning along the trace line in Fig. 10b, no depletion of metallic elements is detected and the austenitic phase is maintained. Hence it is evident that decarburization cannot induce the ferrite phase in Fe–31Mn–9Al–0.87C alloy even with the addition of 6 wt % Cr, which is a ferrite stabilizer [25].

As oxidation proceeds, decarburization reaches a steady state and oxidation is then dominated by metallic element transport. With the presence of voids during the early stage, oxidation will be controlled by the diffusion of manganese due to the relatively higher vapour pressure of manganese over that of either iron or aluminium [8]. The outward growth of manganese oxide is shown schematically in Fig. 9b.

When oxidation proceeds further, say around 12 h, the oxide layer is healed by the less protective oxides such as (Fe, Mn)Al_2O_4 or (Fe, Cr)$_2O_3$ [18]. Due to the fact that manganese acts as the secondary oxygen-getter in this alloy system and because of the fast growth of manganese oxide as mentioned above, the selective oxidation of manganese will play a major role during oxidation. As a result, a manganese depletion zone is formed and the ferrite phase is precipitated. Fig. 9c shows ferrite layer formation due to the selective oxidation of manganese and the carbide formation at the α–γ and α–oxide interfaces.

Because of the low solubility of carbon in the ferrite, carbon originally in the alloy matrix will be redistributed during austenitic decomposition caused by the depletion of manganese. Carbon left in the alloy substrate is either the residual carbon after decarburization or it comes from the alloy matrix due to the carbon gradient after the oxide layer is healed. According to Fig. 1, there are fine and uniformly distributed carbide particles at the ferrite–oxide interface and the number of particles is slightly increased with time. This indicates that some carbon can penetrate through the ferrite layer by volume diffusion. In addition, this also means that the oxide layer is well healed as the carbide is retained beneath the oxide layer. If carbon activity is above the saturation value, breakaway scaling occurs as for alloy B at 800° C and alloy C at 850° C. On the other hand, in the $\alpha \rightarrow \gamma$ transformation region it is argued that the major diffusion path for the redistribution of carbon lies in the defects around the transformation region, such as the boundaries among austenite, ferrite and carbides. As

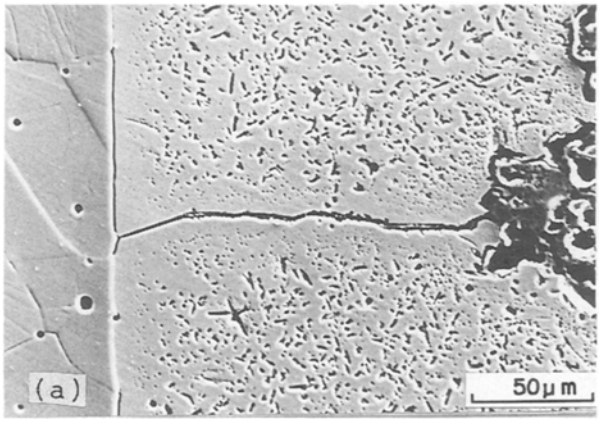

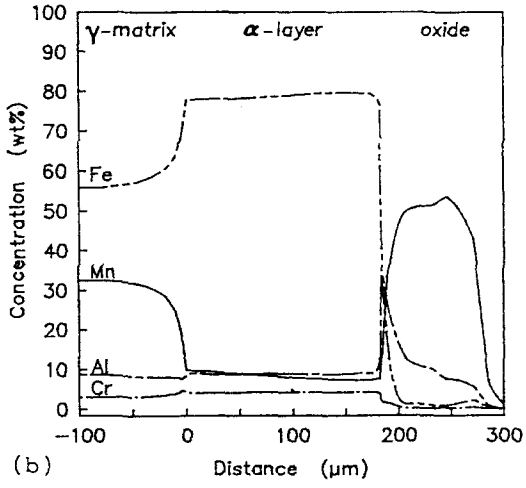

Figure 7 (a) Scanning electron micrograph of alloy C oxidized at 1100° C for 24 h; (b) concentration profiles of metallic elements corresponding to (a).

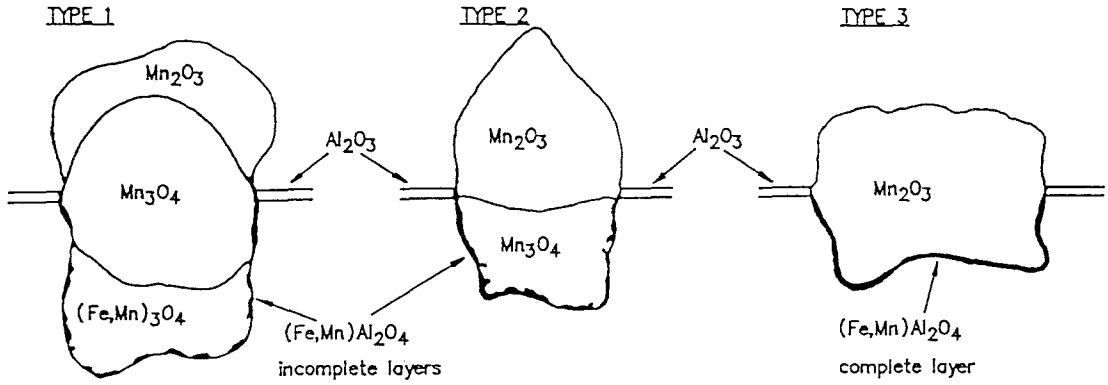

Figure 8 Schematic representation of the oxide structure observed on Fe–Mn–Al alloys containing more than 20% Mn (from [8]).

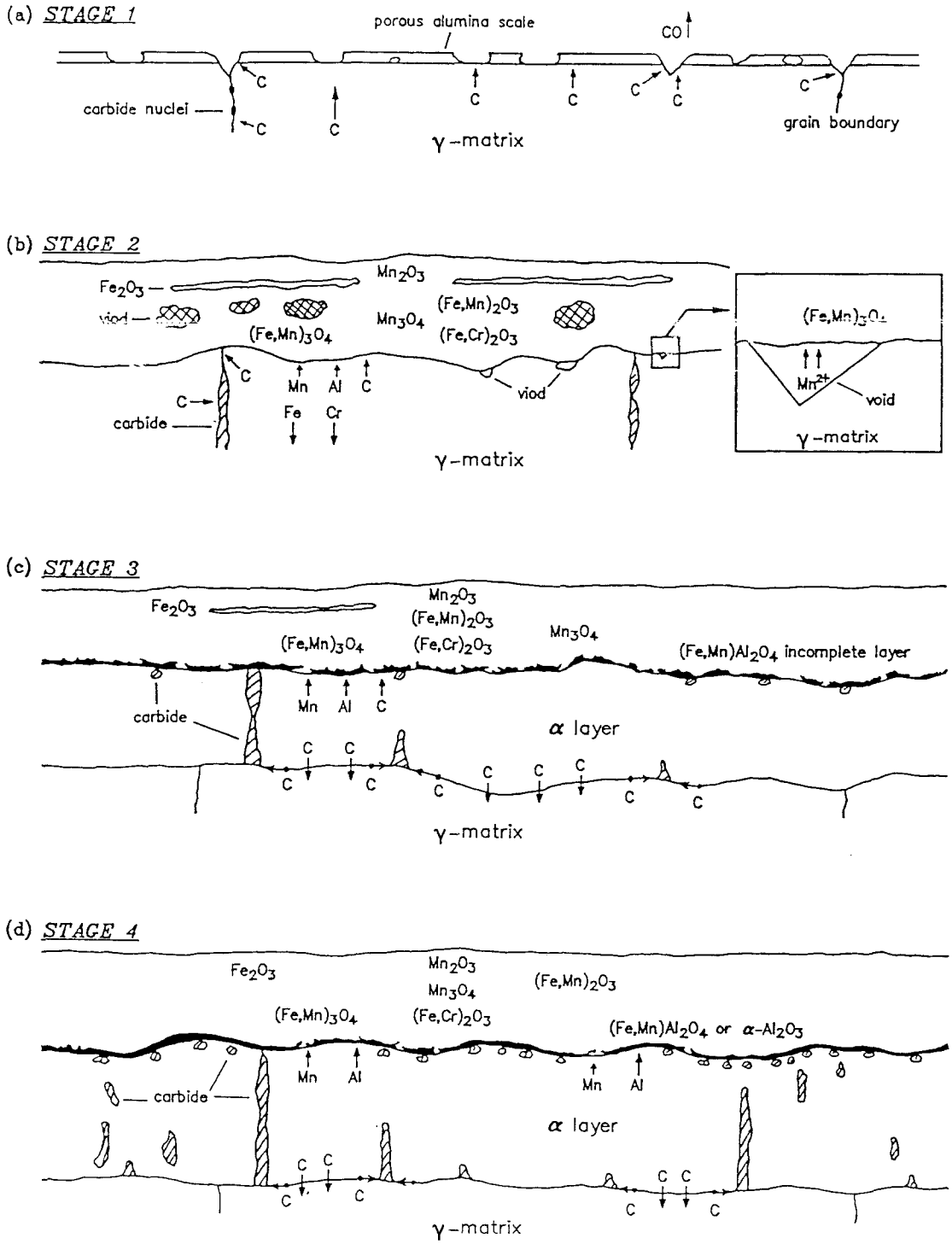

Figure 9 Stages of growth of bulky oxides and the ferrite layer during oxidation of Fe–Mn–Al–C-based alloys. (a) Stage 1: formation of porous initial alumina scale over the alloy surface and carbide formed at the grain boundaries. (b) Stage 2: outward growth of manganese oxide. (c) Stage 3: ferrite layer formed due to the selective oxidation of manganese and carbide formed at the α–γ and α–oxide interfaces. (d) Stage 4: long carbide stringers formed by the migration of α–γ interface.

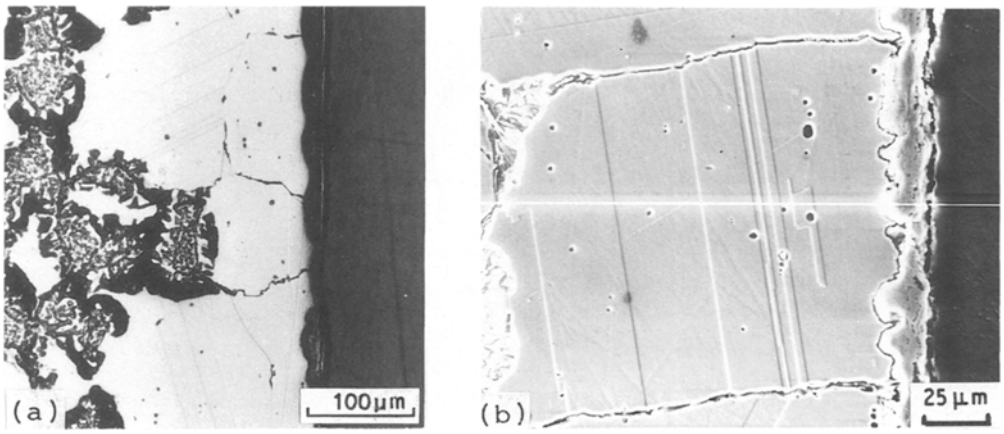

Figure 10 Cross-section of alloy B oxidized at 800° C for 1 h: (a) metallographic picture, (b) SEM image.

the diffusion rate of carbon in ferrite is faster than that in austenite, carbon is piled up toward the austenite as the ferrite is formed, which is similar to austenite decomposition in the Fe–C system [19]. If the carbon content is above the saturation value, carbide would be nucleated at the α–γ interface as shown in Fig. 1. The mobility of carbides is slower than the growth rate of the ferrite layer since isolated carbide stringers or long carbide stringers in contact with the α–γ interface are observed in the ferrite layer. This also implies that diffusion of carbon is along the boundaries as suggested. Due to the large grain size of the specimen after annealing before the oxidation experiments, carbon cannot penetrate further inside the grain. Thus, isolated carbides are formed as carbon migration is perturbed. A schematic representation of this stage of growth is shown in Fig. 9d.

4.1.2. Oxidation at 1000 to 1100° C

At this elevated temperature both the diffusion rates of metallic elements and the growth rates of oxides are enhanced. More metallic elements and the growth rates of oxides are enhanced. More metallic elements are thus introduced into the oxidation during the early stage. Decarburization also occurs in the early stage of oxidation at 1000° C [18]. Due to both the fast diffusion of metallic elements and the appreciable degree of decarburization, voids are formed beneath the healed oxide layer. The non-protective oxide scale with voids is suitable for the selective oxidation of manganese. This is indicated in the concentration profile as seen in Figs 5 and 7b, in which depletion of manganese is shown. As a result, the ferrite layer is formed.

The concentration of carbon caused by redistribution due to the formation of a ferrite layer is also piled up toward the γ side as indicated in Fig. 6. If the activity of carbon is above saturation, Fe_3AlC_x precipitates in the γ gain at the α–γ interface and slightly grows toward the ferrite phase because of the coherent interface between the γ and Fe_3AlC_x. It is found in Figs 4 and 7a that the mobility of Fe_3AlC_x is slower than that of the α–γ interface since Fe_3AlC_x is restricted in the ferrite layer. As the manganese-dominated oxidation proceeds, more manganese is depleted. The driving force for the growth of Fe_3AlC_x is also increased. Carbon required for the growth of Fe_3AlC_x comes from the decomposition of already existing Fe_3Al_x. It is presumed that a moderate degree of decarburization prevails and the decomposition of carbide is favourable. This can be verified by the particle size distribution of Fe_3AlC_x, since larger carbide fringes are mainly in the ferrite grain and grain boundaries, while fine carbides are found between the fringes. As seen in Fig. 7a, it is apparent that a fine carbide layer is present beneath the oxide layer.

At the higher temperature of 1100° C, breakaway scaling also occurs but the scale is healed immediately [18]. The concentration profile of manganese in Fig. 7b shows a gradual decline at the γ side near α–γ interface. This implies that alloy C exhibits a better healing ability and protection at the higher temperature. It appears that diffusional control at the γ side is observed only when the scale is healed and protective, otherwise the concentration of manganese would show a horizontal line at the γ side as seen in Fig. 5.

4.2. Growth of the ferrite layer

Based on the previous discussion, the major differences between the two temperature ranges are related to the distribution profile of carbide precipitation and the controlling mechanism in the early stage of oxidation. In the low temperature range, chromic carbide precipitates in the chromium-containing alloy and carbon-induced oxidation dominates the early stage of oxidation. In the high temperature range, on the other hand, Fe_3AlC_x is precipitated and metallic elements dominate the oxidation in the early stage. The activation energy of the metallic-dominated oxidation is calculated to be 33.48 kcal mol^{-1} (140.17 kJ mol^{-1}) [18], which is comparable with the activation energy of manganese in MnO_{1+x}, 31.3 kcal mol^{-1} (131.0 kJ mol^{-1}) [26]. This indicates that for alloy C the metallic-dominated oxidation is controlled by manganese diffusion in the manganese oxide. This also implies that the formation and the growth of ferrite are in fact dominated by the selective oxidation of manganese as discussed before. It is argued that as aluminium also contributes to oxidation, the activation energy obtained in this study is a little greater than that of pure manganese oxide.

It is proposed that the growth of the ferrite layer is a diffusion-controlled mechanism. Based on Tables II and III, the square of the width of ferrite layer is plotted against time in Fig. 11. A linear relationship

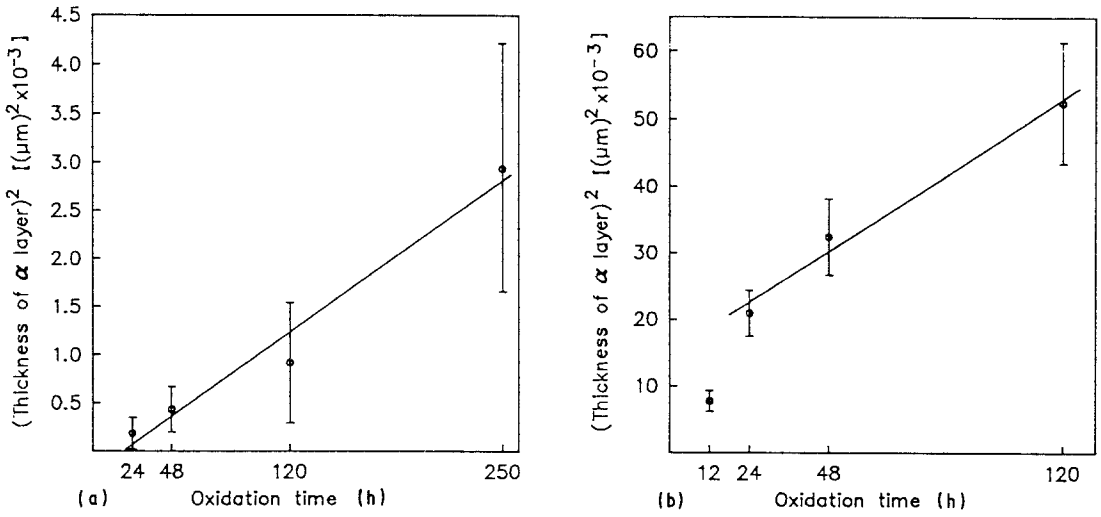

Figure 11 Square of the thickness of the ferrite layer as a function of time for alloy C oxidized at (a) 800, (b) 1000° C.

is found at 800° C as shown in Fig. 11a. A linear relationship is also observed for the last three data points at 1000° C. This indicates that the onset of steady-state growth of the ferrite layer lags behind the early stage of oxidation. Hence the selective oxidation of manganese takes place in the second stage of oxidation, and results in a diffusion-controlled growth of the ferrite layer. On the basis of the diffusion-controlled mechanism [27], the width of the ferrite grows according to a parabolic law

$$X_\alpha^2 = K_\alpha t \quad (1)$$

where X_α is the width of the ferrite layer, K_α is the parabolic rate constant of the growth of the ferrite layer and t is the time. From Fig. 11, K_α values are calculated to be 3.37×10^{-11} and 8.79×10^{-10} cm^2 sec^{-1} for 800 and 1000° C, respectively. According to the Wagner interface wrinkling theory [28, 29], the wavy α–γ interface at 800° C results from competition between the diffusion of iron and manganese at the interface region. Although the diffusivity of manganese is less than that of iron as shown in Table IV [30–34], the ferrite layer is observed to grow parabolically with time. This implies that the driving force for the growth of the layer lies in the selective oxidation of manganese, which predominates over the effect of the self-diffusion of the alloying elements.

4.3. The effects of chromium

By comparing the oxide phases present in three alloys with different contents of chromium at 800° C, the amount of α-Fe_2O_3 is found to decrease as the chromium content is increased. For alloy B with 6 wt % Cr, α-Fe_2O_3 is hardly detected. For alloy C at 1000° C, iron is depleted in the oxide layer based on the X-ray map [4]. This is due to the fact that the addition of chromium can act as an oxygen-getter to stabilize the nucleation and growth of wustite [8]. On the basis of the free energy of formation for oxides [35, 36], the oxidation of iron can be restricted by the presence of chromium. However, there is no effect on manganese since manganese oxide is more stable than chromium oxide. As a result, the width of the ferrite increases as the chromium content is raised. The widths of the ferrite layer are 5, 13 and 25 μm at 800° C for alloys containing 0, 3 and 6 wt % Cr, respectively.

5. Conclusions

1. An oxidation-induced ferrite layer is observed between the oxide layer and the matrix for three austenitic Fe–31Mn–9Al–xCr–0.87C (x = 0, 3 and 6) alloys oxidized in dry air at 800 to 1100° C.

2. The formation and growth of the ferrite layer are controlled by the selective oxidation of manganese.

3. The growth of the ferrite layer is a diffusion-controlled mechanism and the width of the ferrite layer increases with the chromium content in the alloy.

4. The formation and growth of the oxidation-induced ferrite layer can be understood in terms of elemental redistribution due to the carbon migration caused by decarburization and the precipitation of chromium carbides as well as iron aluminium carbides Fe_3AlC_x.

TABLE IV Diffusion coefficients for alloying elements in Fe–Mn–Al–Cr–C alloys

Element	Diffusivity (cm^2 sec^{-1})			Ref.	Remarks
	800° C	1000° C	1100° C		
C	2.3×10^{-8}	2.9×10^{-7}	8.0×10^{-7}	30	Fe–13Mn–1.25C; self-diffusion.
Fe	2.1×10^{-12}	4.1×10^{-10}	3.2×10^{-9}	31	Fe–2.9Cr–0.005C, α-region; volume diffusion.
	1.3×10^{-13}	6.0×10^{-12}	2.6×10^{-10}	31	Fe–2.9Cr–0.005C, γ-region; volume diffusion.
Al	1.0×10^{-11}	7.2×10^{-10}	3.8×10^{-9}	32	Al in Fe; impurity diffusion.
Mn	3.0×10^{-14}	3.3×10^{-12}	2.0×10^{-11}	33	Fe–10.5Mn; tracer diffusion.
Cr	4.0×10^{-12}	2.9×10^{-10}	1.6×10^{-9}	34	Fe–2Cr; self-diffusion.
	3.3×10^{-12}	2.2×10^{-10}	1.1×10^{-9}	34	Fe–6Cr; self-diffusion.

Acknowledgement

The authors are grateful for financial support from the National Science Council, Taiwan under Contract No. NSC 77-0405-E007-15.

References

1. S. K. BANERJI, in Workshop on Trends in Critical Materials Requirements for Steels of the Future–Conservation and Substitution Technology for Chromium, Vanderbilt University, Nashville, USA, October 1982 (Foote Mineral Co., Pennsylvania, FASRAD #82-12).
2. J. P. SAUER, R. A. RAPP and J. P. HIRTH, *Oxid. Met.* **18** (1982) 285.
3. C. H. KAO, C. M. WAN and M. T. JAHN, in Proceedings, "Alternative Alloying for Environmental Resistance", edited by G. R. Smolik and S. K. Banerji, TMS–AIME Annual Meeting in New Orleans (Metallurgical Society, Warrendale, Pennsylvania, 1987) p. 347.
4. J. G. DUH, C. J. LIN, J. W. LEE and C. M. WAN, *ibid.* p. 283.
5. J. G. DUH, C. J. WANG, C. M. WAN and B. S. CHIOU, *ibid.* p. 291.
6. C. J. WANG and J. G. DUH, *J. Mater. Sci.* **23** (1988) 769.
7. P. TOMASZEWICZ and G. R. WALLWORK, *Oxid. Met.* **20** (1983) 75.
8. P. R. S. JACKSON and G. R. WALLWORK, *ibid.* **21** (1984) 135.
9. *Idem*, *ibid.* **20** (1983) 1.
10. C. J. WANG and J. G. DUH, *J. Mater. Sci.* **23** (1988) 3447.
11. J. M. OH, M. J. McNALLAN and W. E. KING, *J. Electrochem. Soc.* **133** (1986) 1042.
12. D. L.DOUGLASS, F. GESMUNDO and C. de ASMUNDIS, *Oxid. Met.* **25** (1985) 235.
13. M. V. C. ARABE and E. M. P. SILVA, in Proceedings, "Alternate Alloying for Environmental Resistance", edited by G. R. Smolik and S. K. Banerji, TMS–AIME Annual Meeting in New Orleans (Metallurgical Society, Warrendale, Pennsylvania, 1987) p. 447.
14. G. R. SMOLIK, J. E. FLINN, D. V. MILEY and G. E. KORTH, *ibid.* p. 307.
15. J. M. OH and M. J. McNALLAN, *J. Electrochem. Soc.* **134** (1987) 1010.
16. J. G. DUH, J. W. LEE and C. J. WANG, *J. Mater. Sci.* **23** (1988) 2649.
17. J. G. DUH and J. W. LEE, *J. Electrochem. Soc.* **136** (1989) 847.
18. C. J. WANG, PhD thesis, National Tsing Hua University, Taiwan (1988).
19. L. S. DARKEN and R. M. FISHER, in "Decomposition of Austenite by Diffusional Processes", edited by V. F. Zackay and H. I. Aaronson (Metallurgical Society, Warrendale, Pennsylvania, 1962) p. 249.
20. G. B. ABDERRAZIK, G. MOULIN, A. M. HUNTTZ and R. BERNERON, *J. Mater. Sci.* **19** (1984) 3173.
21. A. U. MALIK, *Oxid. Met.* **25** (1985) 233.
22. D. CAPLAN, R. J. HUSSEY, G. I. SPROULE and M. J. GRAHAM, *ibid.* **14** (1980) 279.
23. R. A. RAPP, *Met. Trans. A* **15** (1984) 765.
24. J. BAND, A. FERRIER, J. MANENC and J. BENARD, *Oxid. Met.* **9** (1975) 69.
25. E. C. BAIN and H. W. PAXTON, in "Alloying Elements in Steel", 2nd Edn (ASM, Metals Park, Ohio, 1966) p. 6.
26. J. B. PRICE, PhD thesis, Northwestern University (1968) p. 141.
27. B. D. BASTOW, D. P. WHITTLE and G. C. WOOD, *Oxid. Met.* **12** (1978) 413.
28. C. WAGNER, *Corros. Sci.* **103** (1956) 627.
29. G. R. WALLWORK, *Rep. Prog. Phys.* **39** (1976) 401.
30. P. L. GRUZIN, V. I. GRIGORKIN, V. V. MURAL and L. N. MOSKALEVA, *Diffusion Data* **4** (1970) 207.
31. A. M. HUNTZ, P. GUIRALDENG, M. AUCOUTURIER and P. LACOMBE, *ibid.* **4** (1970) 204.
32. A. VIGNES, J. PHILIBERT, M. BADIA and J. LEVASSEUR, *ibid.* **3** (1969) 269.
33. K. NOHARA and K. HIRANO, *Suppl. Trans. Iron Steel Inst. Jpn* **11** (1971) 1267.
34. A. W. LEAK and G. M. LEAK, *Met. Trans.* **10** (1979) 2767.
35. Y. JEANNIN, C. MANNERSKANTZ and F. D. RICHARDSON, *Trans. Met. Soc. AIME* **227** (1963) 300.
36. D. R. STULL and H. PROPHET, in "JANAF Thermochemical Tables", NSRDS-NBS37 (US Department of Commerce, Washington, DC, 1971).

Received 19 August 1988
and accepted 24 July 1989